Asian Journal of Chemistry; Vol. 37, No. 10 (2025), 2397-2405
ASIAN JOURNAL OF CHEMISTRY
https://doi.org/10.14233/ajchem.2025.34199

Structural, Morphological and Electrochemical Properties of Gd doped Fe_3O_4 Nanoparticles for Supercapacitor Applications

J. RAGAVI DURGA*, and C. RAKKAPPAN

Department of Physics, Annamalai University, Annamalai Nagar, Chidambaram-608002, India

*Corresponding author: E-mail: ragavidurga97@gmail.com

Received: 5 June 2025 *Accepted*: 30 August 2025 *Published online*: 30 September 2025 AJC-22123

In this study, Fe_3O_4 and gadolinium-doped Fe_3O_4 nanoparticles were synthesized using the hydrothermal method. The impact of doping on the structural, morphological and optical properties of Gd-Fe_3O_4 was investigated. The XRD analysis indicated that the synthesized samples had a spinel cubic structure and no other secondary phase was detected at Gd-Fe_3O_4 nanoparticles. The FTIR studies demonstrate the presence of characteristic peaks associated with tetrahedral and octahedral vibrations, which support the existence of spinel structure. The nanoscopic phase of the particles size was confirmed by the histogram analysis derived from FESEM images, which ranges from 58 to 62 nm. EDAX analysis was employed to ascertain the distribution of Gd in the Gd-Fe_3O_4 sample. The optical investigations indicate that the indirect bandgaps decrease from 3.8 to 3.6 eV. Cyclic voltammetry revealed the pseudocapacitive behavior of the synthesized materials, with the Gd-Fe_3O_4 electrode exhibiting a significantly higher specific capacitance (692 F g^{-1}) compared to the Fe_3O_4 electrode (295 F g^{-1}).

Keywords: Gadolinium, Nanoparticles, Electrochemical properties, Pseudocapacitance, Cyclic voltammetry, Supercapacitor.

INTRODUCTION

Electrochemical energy storage is a crucial method for addressing the energy issue [1]. The primary electrochemical energy storage devices include metal-air batteries, sodium-ion, lithium-ion batteries, supercapacitors, *etc*. [2-4]. Among these energy storage devices, supercapacitors also known as electrochemical capacitors that serve as a bridge between traditional dielectric capacitors and batteries. Supercapacitors are a viable alternative energy storage technology due to their advantages such as quick charging and discharging, high rate capability, extended cycle life, better reversibility and high-power density [5]. Supercapacitors accumulate energy *via* two distinct mechanisms *viz*. electrical double layer capacitance (EDLC) and pseudocapacitance. Also, the electrochemical performance is mostly determined by their electrode material, which is categorized into three types: conducting polymers, transition metal oxides or hydroxides and carbonaceous materials [6-8].

Transition metal oxides (Co_3O_4, NiO, CuO, MnO_2, *etc*.) are very interesting as pseudocapacitance electrode materials due to their metallic ions are in a multivalent state and their crystal structures allow for fast Faradaic redox reactions [9]. The practical utilization of transition metal oxides in supercapacitors has been severely constrained due to their expensive and hazardous synthesis procedure. Consequently, it is highly vital to engineer advanced electrode materials for supercapacitors that exceed the limitations of previous materials. In this regard, Fe_3O_4 is the most highly theoretically specific capacitance of the group, with a value of 2299 F g^{-1}. Fe_3O_4 is characterized by a wide operating potential range (-1.2 to 0.25 V), high stability in the negative potential range, low toxicity, high abundance and low cost [10,11]. Nevertheless, Fe_3O_4 exhibits poor electrochemical performance and low cycling stability, as a result of its low electrical conductivity and low structural stability during the charge/discharge process, as observed in other metal oxide electrode types. In order to enhance the electron transport properties and obtain a suitable capacitance value, numerous endeavors have been performed to enhance the capacitive performance of Fe_3O_4 by incorporating conductive additives, such as polymers, graphene, carbon material and other composites. Recently, doping cubic spinel ferrites with rare-earth elements (Gd^{3+}, Y^{3+}, Eu^{3+}, Tb^{3+}, Dy^{3+}, *etc*.) structures has the capacity to alter their properties.

Gadolinium (Gd) is a promising material for the supercapacitor electrodes, and its incorporation into Fe_3O_4 significantly enhances pseudocapacitive performance; however, few literature exists on Gd-doped Fe_3O_4, with most studies focusing on the electrochemical and magnetic properties of the nanoparticles [12]. Numerous methods known for the synthesis of nanosized Fe_3O_4 nanoparticles like co-precipitation [13], sol-gel [14], microwave induced combustion [15], evaporation method [16], hydrothermal method [17] and microwave sintering method [18]. Compared to other methods, the hydrothermal technique offers significant advantages, including cost-effectiveness, high purity and superior control over particle size and morphology, leading to enhanced reactivity and performance [19].

The present study reports a hydrothermal synthesis of spherical Fe_3O_4 nanoparticles and explores the incorporation of Gd^{3+} ions into the Fe_3O_4 lattice to enhance electrochemical performance. Gadolinium was selected as a dopant due to its ability to improve specific capacitance, along with its environmental friendliness, low cost and natural abundance. The effects of Gd doping on the structural, morphological and optical properties of Fe_3O_4 nanoparticles were systematically investigated and discussed.

EXPERIMENTAL

Synthesis of Fe_3O_4 and Gd-Fe_3O_4 nanoparticles: In the sample preparation, ferric chloride hexahydrate ($FeCl_3{\cdot}6H_2O$) and ferrous chloride tetrahydrate ($FeCl_2{\cdot}4H_2O$) were utilized in hydrothermal method in an aqueous medium to synthesize Fe_3O_4 sample. All chemicals were of analytical grade and were weighed in the stoichiometric proportions. For sample preparation, 5 mmol of $FeCl_2{\cdot}4H_2O$ and 2 mmol of $FeCl_2{\cdot}6H_2O$ were dissolved separately in 100 mL of deionized water, then mixed and stirred for 30 min. Further, A 1 M NaOH solution was added dropwise to adjust the pH to 12. The mixture was stirred for 1 h, transferred to a 100 mL Teflon-lined stainless-steel autoclave and heated at 180 ºC for 6 h. After cooling to room temperature, the resulting black precipitate was collected, washed with ethanol and dried at 60 ºC for 6 h. The dried product was then calcined at 600 ºC for 4 h and ground into fine powder using an agate mortar. The Gd-doped Fe_3O_4 nanoparticles were synthesized using the same method, with the addition of gadolinium as a dopant.

Characterization techniques: Thermal analysis was analyzed utilizing the NETZSCH-STA 44 F3 Jupiter equipment. The crystal structure and phase purity of Gd doped Fe_3O_4 nanoparticles were studied by XRD pattern through Cu*K*a radiation of wavelength 1.5406 Å (XPertProPW3050/60). The presence of vibrational band was examined by FTIR spectroscopy using Thermo-Nicolet iS5 instrument in the range of 4000-400 cm^{-1}. FESEM was analyzed to investigate the morphological characteristics using the CARL ZEISS-SIGMA 300 apparatus and the compositional analysis was recorded by EDAX spectroscopy coupled with FESEM. The lattice patterns and structure of prepared material were acquired using the FEI Technai G2 20 S-TWIN (TEM). To examine the valance state of the Gd-Fe_3O_4 nanoparticles was employed by ALU-PHI 5000 VER instrument. The optical properties were determined using the JASCO V-670 spectrophotometer. The electrochemical measurement of Gd-Fe_3O_4 electrode was assessed in 1 M KOH electrolyte at room temperature using autolab equipment.

RESULTS AND DISCUSSION

Thermal studies: The TGA analysis was conducted to verify the formation of a crystalline phase of spinel Fe_3O_4 nanoparticles. The TGA graph of the synthesized Fe_3O_4 and Gd-Fe_3O_4 nanoparticles are illustrated in Fig. 1, which allows for the measurement of the both samples resistance to thermal decomposition or degradation. The weight loss of Fe_3O_4 can be classified into two segments: an initial weight loss of 14% below 100 ºC, attributed to the dehydration of residual water moisture, followed by a subsequent weight loss of 4% between 180 ºC and 700 ºC, resulting from an autocatalytic oxidation-reduction reaction. The sample attained weight stability at temp-

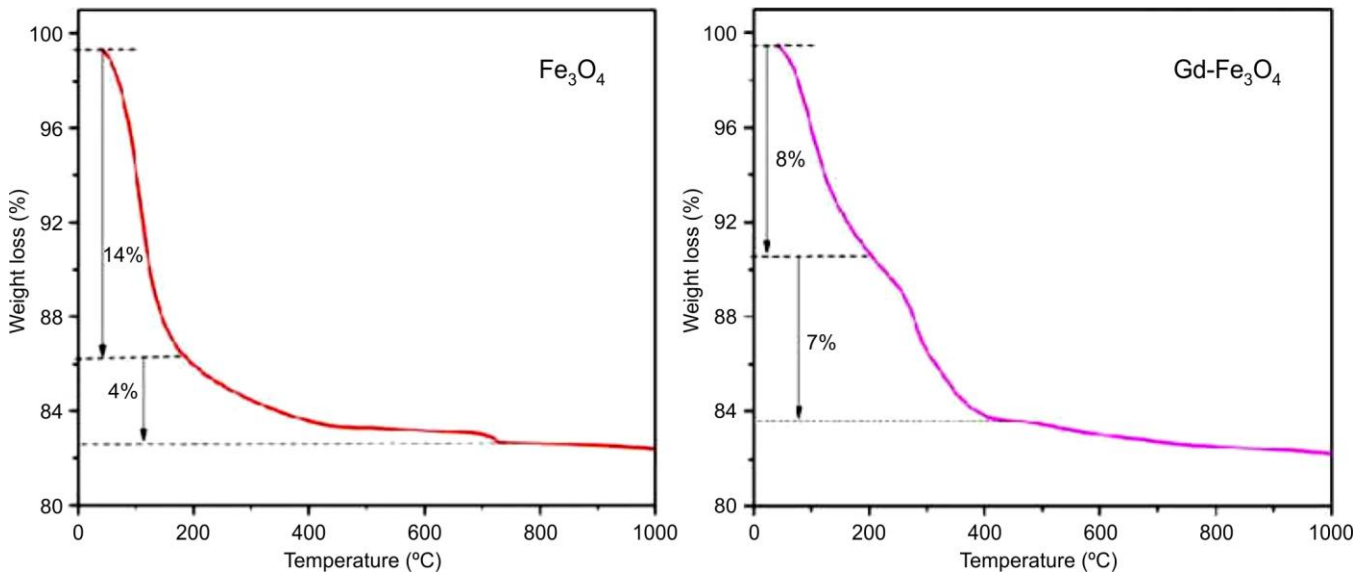

Fig. 1. TGA analysis of as-prepared nanoparticles

eratures exceeding 700 ºC. The TGA plot demonstrated that organic molecules were removed at temperatures over 700 ºC, leading to the elimination of residual reactants and carbonic-eous materials, thereby establishing a stable phase. The TG graph indicated that Gd-Fe_3O_4 sample, weight loss diminished by only 8% and 7%, respectively, in comparison to the undoped sample (18%). Consequently, TGA analysis indicates that thermal stabilization enhanced with the Gd-Fe_3O_4 in the magnetite system [20]. Based on the results, the calcinations temperature was fixed at 600 ºC to obtain sharp and high intensity of Gd doped Fe_3O_4 nanoparticles.

XRD studies: The XRD spectra of Fe_3O_4 and Gd doped Fe_3O_4 nanoparticles are depicted in Fig. 2. The diffraction peaks of all the prepared samples were indexed to spinel cubic structure. The prepared samples had similar XRD patterns that correspond to the standard JCPDS card no. 89-3854. The well-crystalline nature of Fe_3O_4 nanoparticles was implied by the sharp and high intensity of diffraction peaks. The diffraction peaks of the Gd-Fe_3O_4 nanoparticles was observed at (220), (311), (400), (422) and (440), where they correspond to the peak positions of 30.72º, 35.44º, 43.05º, 53.93º and 62.34º, respectively. When compared to Fe_3O_4 sample, the intensity the Gd-Fe_3O_4 sample diffraction peaks intensity was increases. These findings suggested that the crystal structure of Fe_3O_4 nanoparticles was not affected by the Gd doped Fe_3O_4 sample. Furthermore, the lack of secondary peaks suggested that Gd ions were successfully incorporated into the Fe_3O_4 lattice, occupying Co^{2+} without modifying the cubic structure. The crystallite size is determined using Scherrer's formula expressed as follows [21]:

$$D = \frac{0.89\lambda}{\beta \cos\theta} \quad (1)$$

where λ = wavelength; β = the full width at half maximum; D = the crystallite size; and θ = the Bragg's angle. The evaluated crystallite sizes were found to be 55 and 58 nm corresponding to the Fe_3O_4 and Gd-Fe_3O_4 nanoparticles, respectively. The crystallite size increased with Gd-Fe_3O_4 nanoparticles due to the diffraction peaks become sharper. The high-intensity sharp peaks in all prepared samples indicate the crystalline characteristics of Gd-Fe_4O_3, which is advantageous for surface electrochemical processes. Similar observation was reported by Kadian *et al.* [22] and prepared Gd-doped Fe_3O_4 samples were synthesized following the co-precipitation method. The estimated average crystallite size increases with increasing Gd concentrations.

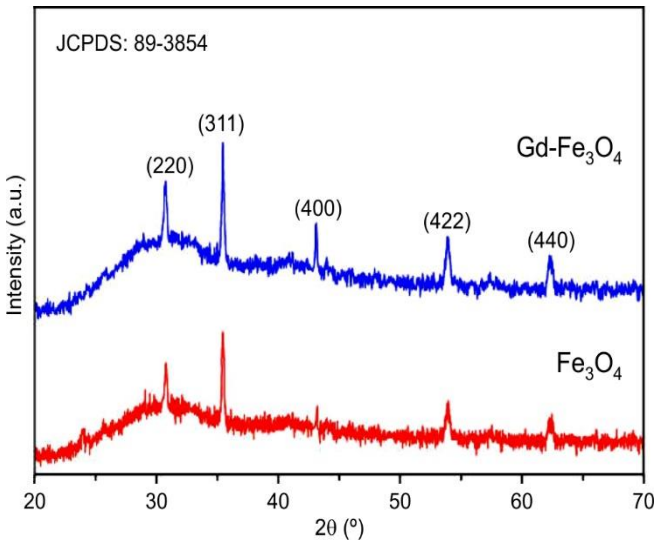

Fig. 2. XRD patterns of Fe_3O_4 and Gd-Fe_3O_4 nanoparticles

FTIR spectral studies: A wide vibration band detected between 3640 and 3000 cm^{-1} is attributed to O–H stretching vibrations in the remaining Gd-substituted hydroxide products, suggesting that the ultrafine particles may physically absorb moisture from the atmosphere [23]. The peak at 1610 cm^{-1} are attributed to the hydroxyl groups of molecular water, specifically the H-O-H bending of the coordinated water [24]. Fig. 3 illustrates that the peaks appears at 1349 and 1118 cm^{-1} correspond to distinct vibrational modes of the carbonate groups resulting from the adsorption of ambient CO_2 [25]. The metal oxygen bond is characterized by the bands observed at 483, 573 and 635 cm^{-1}. Two primary absorption bands were observed at 483 and 573 cm^{-1}, which correspond to the stretching vibrations of the octahedral and tetrahedral sited metal-oxygen (Gd/Fe-O) ions, respectively [26]. The variation in bond length between the metal and oxygen atoms at the octahedral and tetrahedral sites, as indicated by the XRD data, produces two distinct IR bands at varying wavenumbers. Both absorption bands are typical representations of spinel structure. The band associated with the octahedral site becomes broader and exhibits a minor shift in position in comparison to the pure ferrite sample as the concentration of Gd^{3+}. This may be attributed to the alteration in bond lengths between the tetrahedral and octahedral sites, as well as the lattice parameters of the cubic structure, which were also altered by the doping [27].

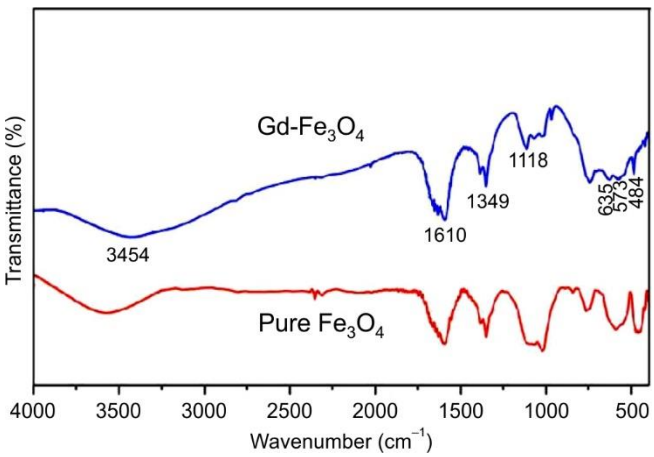

Fig. 3. FTIR spectra of Fe_3O_4 and Gd-Fe_3O_4 nanoparticles

Morphological studies: FESEM analysis was employed to analyze the microstructure and morphological properties of Fe_3O_4 and Gd-Fe_3O_4 nanoparticles. The Fe_3O_4 sample had spherical particles with attached each other and formed cluster like structures (Fig. 4a-b). The incorporation of Gd ions into Fe_3O_4 lattice resulted in noticeable the morphological changes. Micrographs of the Gd–Fe_3O_4 sample revealed well-defined spherical particles uniformly distributed across the surface (Fig. 4d-e). The particles aggregate as a result of their magnetic interactions with one another. These agglomerates are held together by magnetic forces or comparatively weak van der

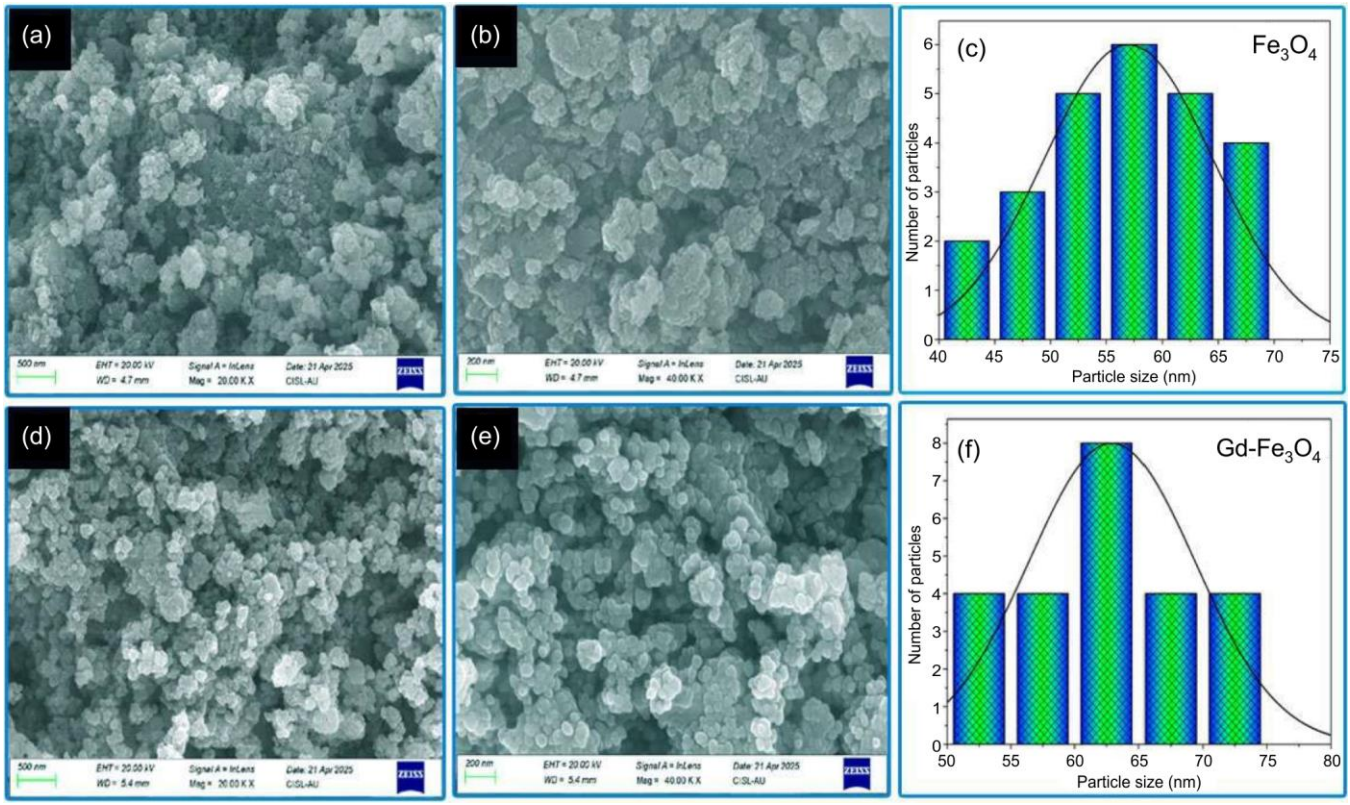

Fig. 4. FESEM images (a,b) Fe_3O_4 nanoparticles, (d,e) Gd-Fe_3O_4 nanoparticles and corresponding histogram images (c,f)

Waal's forces [28]. It is observed that the Gd concentration in ferrite results in changes to the grain boundaries. The adaptability of grain borders is crucial for grain growth; hence, the incorporation of Gd^{3+} ions into the ferrite lattice enhanced the grain boundaries owing to its bigger atomic size [29,30]. The Image J software is used to determine the average grain size from these micrographs. The average particle size of the prepared samples was analyzed from the histogram, as shown in Fig. 4(c-f). The estimated values are 58 nm and 62 nm for Fe_3O_4 and Gd-Fe_3O_4 nanoparticles, respectively. The average particle size values are slightly greater than the crystallite size determined from the XRD data. This result revealed that each particle is composed of multiple crystallites.

The EDAX spectra of the pure Fe_3O_4 and Gd-Fe_3O_4 nanoparticles are displayed in Fig. 5a-b. The Gd-Fe_3O_4 samples exhibited the presence of Fe, O and Gd elements, whereas the pure sample contained only Fe and O elements, which suggests that the synthesized nanoparticles were of high purity.

HRTEM analysis: In order to examine the structure and size of the synthesized nanoparticles, HRTEM images were utilized. A spherical shape was visible in the HRTEM photographs of the Gd-Fe_3O_4 nanoparticles. Fig. 6c show the lattice spacing value for doped sample, with a measured value of 0.253 nm that agreed with the (311) crystallographic plane of the Gd-Fe_3O_4 nanoparticles. The determined *d*-spacing values were in close agreement with the standard JCPDS card no. 89-3854. HRTEM images revealed the selected area diffraction pattern (SAED) of Gd doped sample, which showed strong diffraction with dots and were polycrystalline in nature (Fig. 6d). The observed findings were in good agreement with the FESEM results.

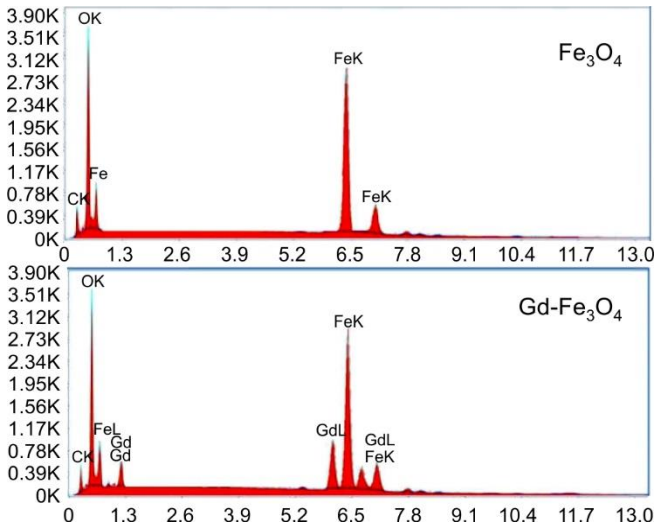

Fig. 5. EDAX spectrum of prepared nanoparticles

XPS analysis: Fig. 7a shows the spectrum of Gd-Fe_3O_4 nanoparticles indicates the existence of Gd 3d, Fe 2p and O 1s elements. The two high-resolution significant characteristics peaks, Fe $2p_{1/2}$ and $Fe2p_{3/2}$, are shown in Fig. 7b at 711.5 and 725.2 eV, respectively [31]. The presence of peak indicates that the produced phase is maghemite, with all iron content oxidized to Fe^{2+} and Fe^{3+} ions. The low energy peak was also located at 711.5 eV, indicating Fe^{3+} ions occupying in the octahedral sites. Fig. 7c presents a high-resolution figure illustrating the peaks of Gd^{4+}. The elevated energy peak (Gd $3d_{5/2}$) is detected at 1185.6 eV, while the low energy peaks (Gd 4d) observed at 142.5 eV and 148.5 eV for Gd $4d_{5/2}$ and

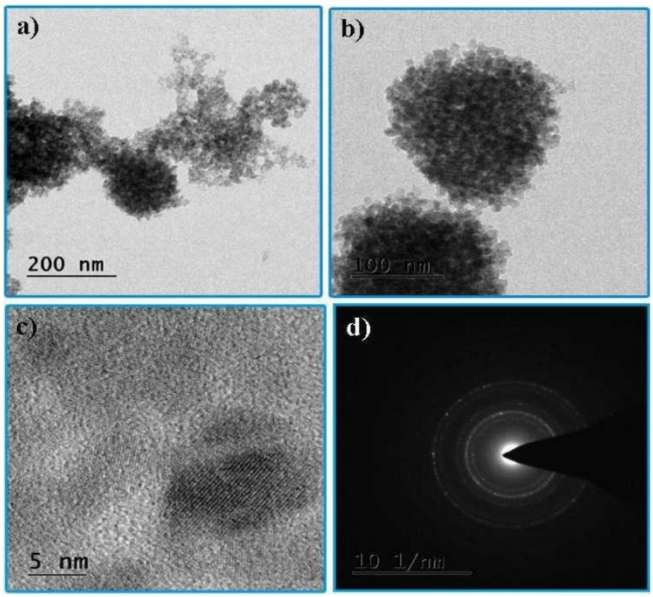

Fig. 6. HRTEM analysis of Gd-Fe_3O_4 nanoparticles (a,b) images (c) lattice spacing, (d) SAED pattern

Gd $4d_{3/2}$, respectively [32]. The O 1s XPS spectra of Gd-Fe_3O_4 nanoparticles are shown in Fig. 7d. Zhang *et al.* [33] also reported the deconvolution and indexing of the peak located at 530.3 eV. It is formed by the incorporation of oxygen into the lattice, oxygen in the dangling bonds at the surface of the particles and adsorbed oxygen.

Optical studies: The UV-visible absorption spectra of the Fe_3O_4 and Gd-Fe_3O_4 samples fall between the 200 to 800 nm ranges (Fig. 8a). From the spectra, a high absorption peak is found at 270 nm for both samples. It is observed that Gd-Fe_3O_4 sample, the visible light absorption efficiency decreases in the range between 200-500 nm. The absorbance intensity is higher for Fe_3O_4 and lower for the Gd-Fe_3O_4 sample, which has presence of Gd^{3+} ions. The absorbance intensity of nanomaterials in this region is reported to be influenced by a variety of factors, including the size of the crystal, surface roughness and the nature of substituting materials. In addition, the hypochromic effect may be responsible for the reduction in absorption intensity, as it induces certain groups that distort the chromophore [34] (atom or group that determines the colour of a compound).

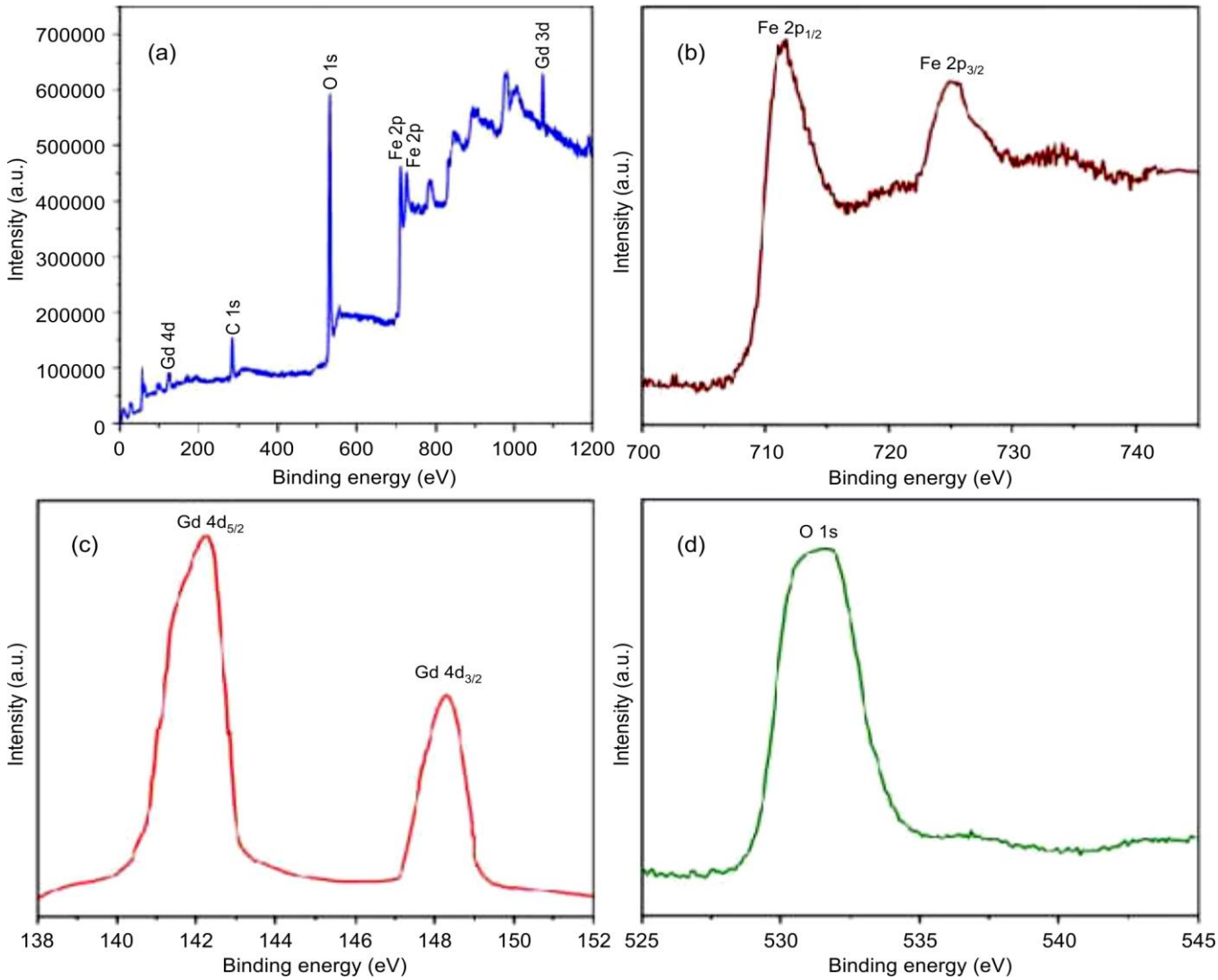

Fig. 7. XPS spectrum of Gd-Fe_3O_4 nanoparticles (a) survey scan (b) Fe 2p (c) Gd 4d (d) O 1s

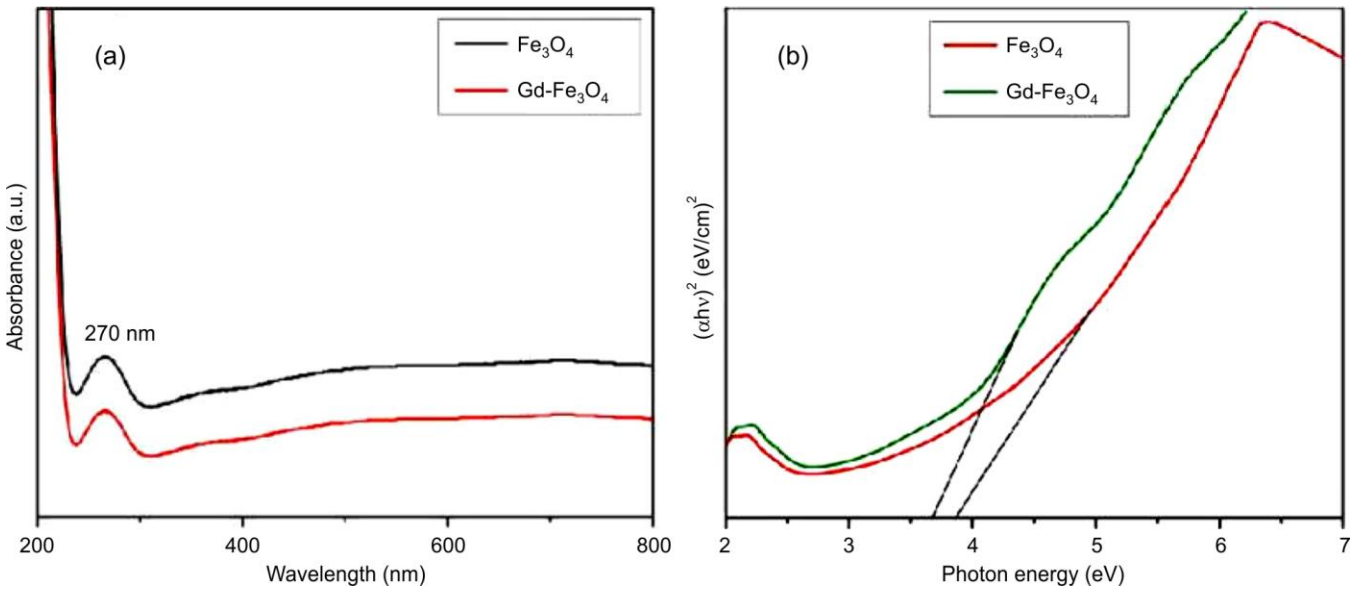

Fig. 8. Optical properties of Fe_3O_4 and Gd-Fe_3O_4 nanoparticles (a) UV-Vis (b) bandgap

The bandgap values of prepared samples were calculated by using the Tauc's equation [35]:

$$\alpha h\nu = A(h\nu - E_g)^n \quad (2)$$

where hν = photon energy; E_g = the optical bandgap of the products; A = constant; and n = 1/2, for direct bandgap semiconductor. Fig. 8b represents the optical bandgap of Fe_3O_4 and Gd-Fe_3O_4 samples and plots the linear part of $(ahv)^2$ on the *y*-axis *versus* hν on the *x*-axis. The estimated bandgap values are found to be 3.8 eV and 3.6 eV for Fe_3O_4 and Gd-Fe_3O_4 nanoparticles, respectively. As a result, Fe_3O_4 sample exhibits the high values of indirect band gap energy, attributed to the orbital overlap between the Fe 3d and O 2p energy states. The band gap decreases with increasing Gd^{3+} concentration, as Gd doping introduces a new donor energy level (4*f* state) just below the Fe 3d conduction band. The interaction between the Gd 4f states and the O 2p orbitals in the valence band enhances charge transfer from the Gd^{3+} energy levels to the Fe 3d conduction band, thereby facilitating the improved charge migration [36].

Electrochemical analysis

Cyclic voltammetry: The electrochemical performance of the synthesized Fe_3O_4 and Gd-Fe_3O_4 electrodes were evaluated using cyclic voltammetry (CV), galvanostatic charge-discharge (GCD) and electrochemical impedance spectroscopy (EIS). Cyclic voltammetry was utilized to determine the capacitance of the Fe_3O_4 and Gd-Fe_3O_4 nanoparticles based on working electrode in a three-electrode configuration with 1 M KOH as electrolyte. The working electrode was prepared by coating Fe_3O_4 and Gd-Fe_3O_4 nanoparticles onto nickel foam, while a platinum wire served as the counter electrode and Ag/AgCl was used as the reference electrode. Fig. 9a depicts the CV profiles of the constructed working electrode throughout a potential range of 0 to 0.3 V at various scan rates 5-100

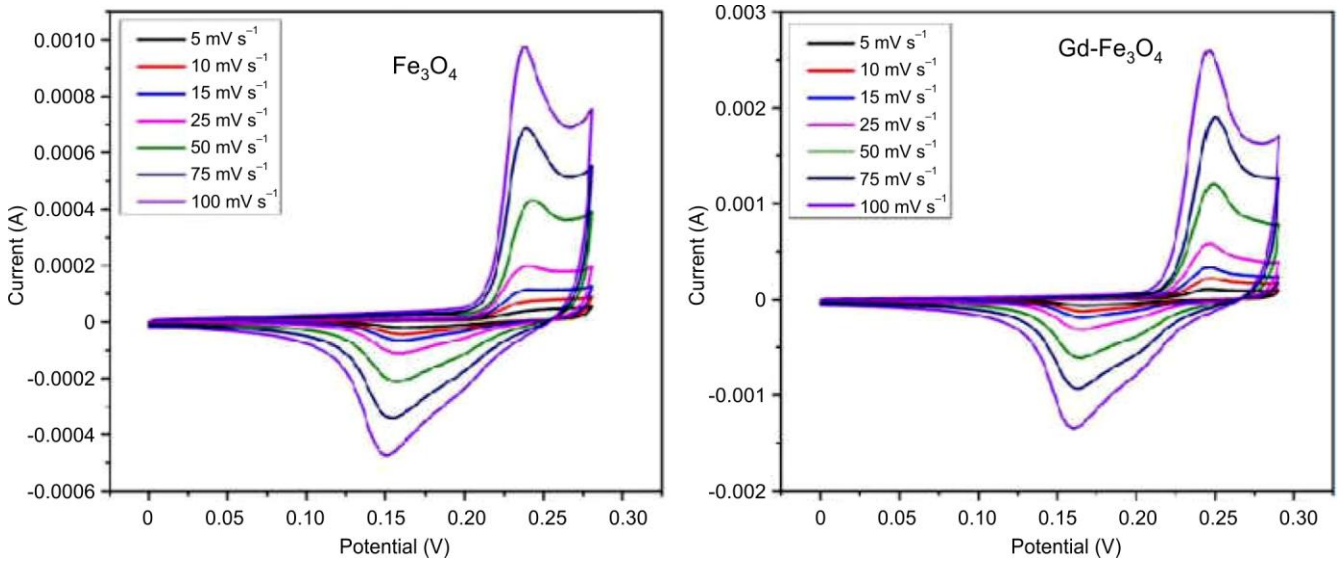

Fig. 9. Cyclic voltammetry of Fe_3O_4 and Gd-Fe_3O_3 nanoparticles

mV/s. The CV curves indicated the prepared electrodes have pseudocapacitive properties, which differed from the electric double-layer capacitance. As the scan rate increases, the peak current density and the position of the redox peaks shift, reflecting rapid ion diffusion and absorption in the electrodes. Fig. 9b also displays the CV profiles of working electrodes fabricated from Fe_3O_4 and Gd-Fe_3O_4 nanoparticles. The Gd-Fe_3O_4 electrode demonstrated superior supercapacitive activity, as evidenced by its larger anodic and cathodic current responses. The area under the current potential curves was integrated to estimate the capacitance values of the two working electrodes from the CV profiles [37].

$$C_s = \frac{\int I.dv}{m \times s \times V} \quad (3)$$

where I·dv is the charge obtained from the CV curves, 'm' is the mass of the active material in the electrode (mg), 'v' is potential window and 's' is the scan rate (mV/s). The specific capacitance values of Fe_3O_4 obtained from the CV curves were 295, 280, 254, 235, 216, 203 and 181 F g^{-1} at scan rates of 5, 10, 15, 25, 50, 75 and 100 mV s^{-1}, respectively. On the other hand, Gd-Fe_3O_4 electrode exhibited the capacitance values of 692, 685, 658, 643, 620, 612 and 590 F g^{-1} at scan rates of 5, 10, 15, 25, 50, 75 and 100 mV s^{-1}, respectively. Moreover, the specific capacitance falls as the scan rate increases. Ions from the electrolyte solution have sufficient time to reach the electrode at modest scan rates and can access materials on both the inner and outer surfaces. Consequently, the electrode's surface may accumulate a substantial quantity of charges, resulting in a high specific capacitance. The specific capacitance was measured at its lowest value due to the fact that the electrode surface experiences a decrease in interaction opportunities with ions and electrons as the scan rate increases [38].

Charging/discharging analysis: The electrochemical performance of pure Fe_3O_4 and Gd-Fe_3O_4 electrodes was investigated using galvanostatic charge-discharge tests. Fig. 10a-b shows the charging and discharging curves of produced electrodes with current densities ranging from 1 to 5 A g^{-1}. The pure Fe_3O_4 electrode displays pseudocapacitance properties, as seen by the consistent fall in the charge-discharge curve duration. This figure distinctly shown that the charging-discharging duration of the Gd-Fe_3O_4 electrode is considerably longer than that of pure electrode. Furthermore, both electrodes demonstrate a linear variation in potential throughout the charging and discharging phases, characterized by an almost triangular shape, which signifies enhanced supercapacitor performance. The specific capacitance was calculated using cyclic voltammetry using the following formula [39]:

$$Cs = \frac{i\Delta t}{\Delta V m} \quad (4)$$

where i denoted the discharge current; m denoted the mass of active material; Δt denoted the discharge time; and ΔV denoted the potential change during the discharge. The measured capacitance (Csp) values of the Fe_3O_4 electrode showed 290, 265, 246, 213 and 175 F g^{-1} for various current densities of 1, 2, 3, 4 and 5 Ag^{-1}, respectively. Subsequently, the Gd-Fe_3O_4 electrode exhibited specific capacitance values of 716, 654, 540, 382 and 290 F g^{-1} for different current densities of 1, 2, 3, 4 and 5 A g^{-1}, respectively. At a low current density, ions were able to access nearly all of the active sites in the electrode material. However, at a high current density, ions were able to only reach the surface of the electrode material. The GCD results suggest that the Gd-Fe_3O_4 electrode has a higher specific capacitance than the Fe_3O_4 electrode. This is likely due to the increased electrical conductivity that results from the integration of Gd into the Fe_3O_4 nanostructures [40].

Electrochemical impedance spectroscopy (EIS) analysis: The impedance behaviour is determined by fundamental electrochemical processes occurring across low, medium and high frequency ranges. The impedance of a supercapacitor is intermediate between that of a capacitor and that of a resistor. The electrochemical system functions more like a resistor at elevated frequencies, while it exhibits characteristics similar to a capacitor at low frequencies. The Nyquist graphs for Fe_3O_4 and Gd-Fe_3O_4 electrodes are depicted in Fig. 11. In the

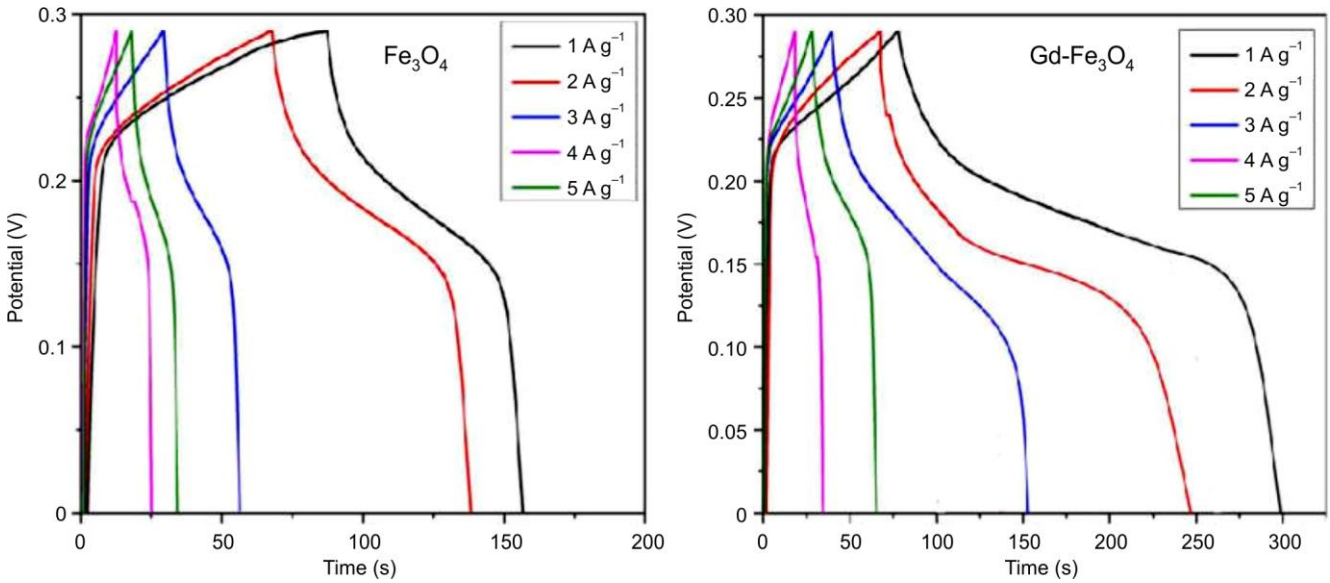

Fig. 10. Galvanostatic charge and discharge profile of Fe_3O_4 and Gd-Fe_3O_4 nanoparticles

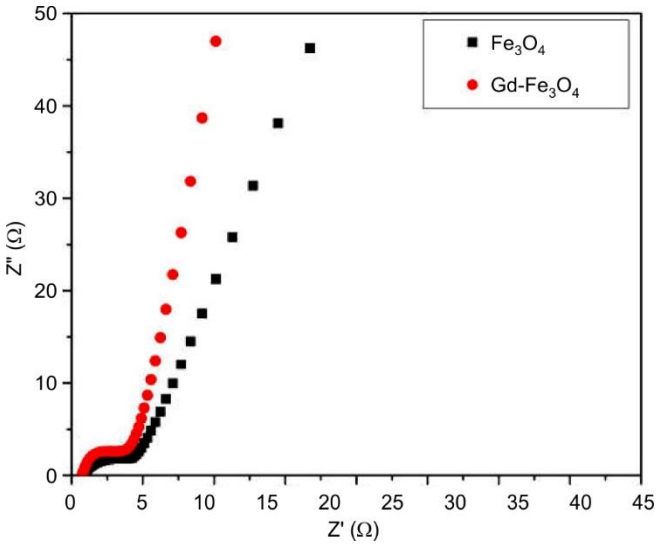

Fig. 11. EIS spectrum of Fe_3O_4 and Gd-Fe_3O_4 nanoparticles

Nyquist plots of synthesized nanoparticles, semicircles and straight lines are observed at the lower and higher frequencies, respectively. The EIS spectrum demonstrates that the diameter of the half-circle for the Gd-Fe_3O_4 electrode is smaller than that of the pure electrode. This difference may be attributed to the pure electrode's higher conductivity. Furthermore, the vertical line is the result of the diffusion of ions between the electrode surface and the electrolyte. This suggests that the electrodes are approaching the characteristics of an ideal capacitor. The computed R_{ct} values for Fe_3O_4 and Gd-Fe_3O_4 were 3.5 and 2.4 Ω, respectively. The results show that the electrical conductivity of Gd-Fe_3O_4 nanoparticles is lower than that of Fe_3O_4. These results suggested that the low resistance and good ion responsiveness, which are due to the material's high purity, metal ion doping and better crystallinity.

Conclusion

In current study, Fe_3O_4 and Gd-Fe_3O_4 nanoparticles were successfully synthesized using the hydrothermal technique. The structural feature was examined using XRD studies, which indicated the nanoparticles were spinel cubic structure. The FT-IR confirmed the spinel structure of the prepared samples by revealing two primary absorbance peaks related to the stretching vibrations of tetrahedral and octahedral metal-oxygen ions, at around 573 and 484 cm^{-1}, respectively. The FESEM and HRTEM images showed the prepared samples were spherical-like structures. The XPS studies revealed the existence the oxidation state of Gd was +3. UV-Vis spectroscopic investigation shows that the intensity of Gd-Fe_3O_4 decreases compared to Fe_3O_4 nanoparticles due to the hypochromic effect. Electrochemical measurements proved that the Gd-Fe_3O_4electrode had a higher capacitance value of 692 F g^{-1} than the pure Fe_3O_4 sample. As a result, Gd doped Fe_3O_4 nanoparticles suggested the increased specific capacitance, making them a promising candidate for energy storage applications.

CONFLICT OF INTEREST

The authors declare that there is no conflict of interests regarding the publication of this article.

REFERENCES

1. M.H. Taabodi, T. Niknam, S.M. Sharifhosseini, H.A. Aghajari and S. Shojaeiyan, *J. Power Sources*, **641**, 236832 (2025); https://doi.org/10.1016/j.jpowsour.2025.236832
2. G. Zubi, R. Dufo-López, M. Carvalho and G. Pasaoglu, *Renew. Sustain. Energy Rev.*, **89**, 292 (2018); https://doi.org/10.1016/j.rser.2018.03.002
3. M. Salado and E. Lizundia, *Mater. Today Energy*, **28**, 101064 (2022); https://doi.org/10.1016/j.mtener.2022.101064
4. L. Liu, X. Zhang, Y. Liu and X. Gong, *ACS Appl. Electron. Mater.*, **7**, 2233 (2025); https://doi.org/10.1021/acsaelm.5c00069
5. K. Chen, S. Song and D. Xue, *J. Mater. Chem. A Mater. Energy Sustain.*, **3**, 2441 (2015); https://doi.org/10.1039/C4TA06989G
6. K.W. Qiu, H.L. Yan, D.Y. Zhang, Y. Lu, J.B. Cheng, W.Q. Zhao, C.L. Wang, Y.H. Zhang, X.M. Liu, C.W. Cheng and Y.S. Luo, *Electrochim. Acta*, **141**, 248 (2014); https://doi.org/10.1016/j.electacta.2014.07.074
7. S.H. Kazemi, A. Asghari and M.A. Kiani, *Electrochim. Acta*, **138**, 9 (2014); https://doi.org/10.1016/j.electacta.2014.06.094
8. J. Xu, L. Gao, J.Y. Cao, W.C. Wang and Z.D. Chen, *Electrochim. Acta*, **56**, 732 (2010); https://doi.org/10.1016/j.electacta.2010.09.092
9. M. Aghazadeh and M.R. Ganjali, *J. Mater. Sci. Mater. Electron.*, **29**, 4981 (2018); https://doi.org/10.1007/s10854-017-8459-0
10. S.C. Pang, W.H. Khoh and S.F. Chin, *J. Mater. Sci.*, **45**, 5598 (2010); https://doi.org/10.1007/s10853-010-4622-1
11. V.D. Nithya and N.S. Arul, *J. Mater. Chem. A Mater. Energy Sustain.*, **4**, 10767 (2016); https://doi.org/10.1039/C6TA02582J
12. P. Akhtar, M.N. Akhtar, M.A. Baqir, A. Ahmad, M.U. Khallidoon, M. Farhan and M.A. Khan, *J. Mater. Sci. Mater. Electron.*, **32**, 7692 (2021); https://doi.org/10.1007/s10854-021-05487-4
13. H. Mohammadi, E. Nekobahr, J. Akhtari, M. Saeedi, J. Akbari and F. Fathi, *Toxicol. Rep.*, **8**, 331 (2021); https://doi.org/10.1016/j.toxrep.2021.01.012
14. G.H. Chen and H.S. Chen, *ACS Appl. Nano Mater.*, **3**, 8858 (2020); https://doi.org/10.1021/acsanm.0c01634
15. A. Căpraru, E.A. Moacă, C. Păcurariu, R. Ianoș, R. Lazău and L. Barbu Tudoran, *Powder Technol.*, **394**, 1026 (2021); https://doi.org/10.1016/j.powtec.2021.08.093
16. R. Fu, X. Jin, J. Liang, W. Zheng, J. Zhuang and W. Yang, *J. Mater. Chem.*, **21**, 15352 (2011); https://doi.org/10.1039/c1jm11883h
17. K. Hedayati, M. Goodarzi and D. Ghanbari, *J. Nanostruct.*, **7**, 32 (2017); https://doi.org/10.22052/jns.2017.01.004
18. N. Kamboj, A. Betal, M. Majumder, S. Sahu and R.K. Metre, *Inorg. Chem.*, **62**, 4170 (2023); https://doi.org/10.1021/acs.inorgchem.2c04264
19. P. Elayarani, T. Sumathi and G. Sivakumar, *J. Mater. Sci. Mater. Electron.*, **35**, 211 (2024); https://doi.org/10.1007/s10854-023-11884-8
20. K.P. Hazarika, R. Fopase, L.M. Pandey and J.P. Borah, *Physica B*, **645**, 414237 (2022); https://doi.org/10.1016/j.physb.2022.414237
21. T. Munawar, S. Yasmeen, M. Hasan, K. Mahmood, A. Hussain, A. Ali, M.I. Arshad and F. Iqbal, *Ceram. Int.*, **46**, 11101 (2020); https://doi.org/10.1016/j.ceramint.2020.01.130
22. N. Kadian, R. Kumari, A. Panchal, J. Dalal and D. Padalia, *J. Alloys Compd.*, **960**, 170811 (2023); https://doi.org/10.1016/j.jallcom.2023.170811
23. S. Xing, Z. Zhou, Z. Ma and Y. Wu, *Appl. Catal. B*, **107**, 386 (2011); https://doi.org/10.1016/j.apcatb.2011.08.002
24. S. Kumari, E. Sharma, J. Verma, J. Dalal and A. Kumar, *Ceram. Int.*, **49**, 20185 (2023); https://doi.org/10.1016/j.ceramint.2023.03.142
25. G. Boopathi, G.G. Karthikeyan, S.M. Jaimohan, A. Pandurangan and A.L.F. de Barros, *Phy. Chem. C*, **122**, 9257 (2018); https://doi.org/10.1021/acs.jpcc.7b11643

26. S.V. Ganachari, R. Bhat, R. Deshpande and A. Venkataraman, *Recent Res. Sci. Technol.*, **4**, 50 (2012).
27. J. Liu, T. Xu, M. Gong, F. Yu and Y. Fu, *J. Membr. Sci.*, **283**, 190 (2006); https://doi.org/10.1016/j.memsci.2006.06.027
28. J. Jiang and Y.-M. Yang, *Mater. Sci. Technol.*, **25**, 415 (2009); https://doi.org/10.1179/174328408X296006
29. J.G. Kang, B.K. Min and Y. Sohn, *Ceram. Int.*, **41**, 1243 (2015); https://doi.org/10.1016/j.ceramint.2014.09.053
30. A.B. Gadkari, T.J. Shinde and P.N. Vasambekar, *Mater. Chem. Phys.*, **114**, 505 (2009); https://doi.org/10.1016/j.matchemphys.2008.11.011
31. H.G. Cha, M.J. Kang, I.C. Hwang, H. Kim, K.B. Yoon and Y.S. Kang, *Chem. Commun.*, **51**, 6407 (2015); https://doi.org/10.1039/C5CC00200A
32. A.M. Faramawy, H. Elsayed, H.M. Elsayed, A.A. Sattar, Y.W. Getahun, A.A. El-Gendy and H. Kahil, *J. Alloys Compd.*, **974**, 172845 (2024); https://doi.org/10.1016/j.jallcom.2023.172845
33. C. Zhang, Q. Wu, X. Ke, Y. Ren, S. Xue, and H. Wang, *Solar Energy*, **135**, 274 (2016); https://doi.org/10.1016/j.solener.2016.06.007
34. L.D.S. Yadav, Organic Spectroscopy, Springer Netherlands, Dordrecht (2005).
35. S. Khashan, S. Dagher, N. Tit, A. Alazzam and I. Obaidat, *Surf. Coat. Tech.*, **322**, 92 (2017); https://doi.org/10.1016/j.surfcoat.2017.05.045
36. S.B. Patil, H.S. Bhojya Naik, G. Nagaraju, R. Viswanath and S.K. Rashmi, *Eur. Phys. J. Plus*, **132**, 328 (2017); https://doi.org/10.1140/epjp/i2017-11602-x
37. S. Sivakumar and L.N. Prabu, *Inorg. Chem. Commun.*, **147**, 110247 (2023); https://doi.org/10.1016/j.inoche.2022.110247
38. B.C. Kim, C. Justin Raj, W.-J. Cho, W.-G. Lee, H.T. Jeong and K.H. Yu, *J. Alloys Compd.*, **617**, 491 (2014); https://doi.org/10.1016/j.jallcom.2014.08.018
39. J. Li, Y. Ren, S. Wang, Z. Ren and J. Yu, *Appl. Mater. Today*, **3**, 63 (2016); https://doi.org/10.1016/j.apmt.2016.03.003
40. Y. Xu, Y. Zhang, X. Song and H. Liu, *Funct. Mater. Lett.*, **12**, 1950019 (2019); https://doi.org/10.1142/S179360471950019X